Fermi surface nesting and magnetic structure of $ErGa_3$

M. Biasini*,† and G. Ferro*
ENEA, Via don Fiammelli, 2 40129 Bologna, Italy

G. Kontrym-Sznajd and A. Czopnik
Trzebiatowski Institute of Low Temperature and Structure Research, P.O.Box 937 Wroclaw, Poland
(Received 15 February 2002; revised manuscript received 21 May 2002; published 30 August 2002)

A three-dimensional mapping of the Fermi surface (FS) of the rare-earth compound $ErGa_3$ was determined via measurements of the angular correlation of the electron–positron annihilation radiation. The topology of the electronlike FS does show nesting properties which are consistent with the modulated antiferromagnetic structure of the system. We determine the density of states at the Fermi energy $N(E_F)$ and the electronic contribution to the gamma constant to be $N(E_F)=16$ states/ Ryd /cell and $\gamma=2.7$ (mJ/mol K^2), respectively.

DOI: 10.1103/PhysRevB.66.075126 PACS number(s): 71.18.+y, 75.10.Lp, 78.70.Bj

I. INTRODUCTION

The rare-earth (RE)–Ga_3 compounds $ErGa_3$ and $TmGa_3$, crystallizing in the cubic $AuCu_3$-type structure, constitute an interesting subject for their magnetic properties. In these systems, the field dependence of the magnetization and the experimental studies of the Fermi surface[1–6] can be interpreted applying the standard lanthanides picture, where the $4f$ electrons are modelled by local atomiclike orbitals. Although the validity of this description (denoted in the following as *f-core*) is widely discussed, it can be assumed as a fairly realistic starting assumption. The standard lanthanides model assumes that the magnetic coupling between the $4f$ electrons is carried out indirectly via polarization of the conduction electrons, according to the Ruderman–Kittel–Kasuya–Yosida (RKKY) theory. Long ago, it was proposed that, thanks to the interplay between local moments and conduction electrons, the Fermi surface (FS) topology may control the magnetic properties of rare earth compounds.[7] This action can be understood by looking at the expression of the Fourier transformed exchange coupling constant $J(\boldsymbol{q})$,[8,9]

$$J(\boldsymbol{q}) \propto \sum_{k} I(\boldsymbol{k},\boldsymbol{q}) \frac{f^0(\boldsymbol{k}) - f^0(\boldsymbol{k}+\boldsymbol{q})}{E(\boldsymbol{k}+\boldsymbol{q}) - E(\boldsymbol{k})}. \tag{1}$$

Here the summation is over the $\boldsymbol{k}$ electron states, $f^0(\boldsymbol{k})$ is the Fermi–Dirac distribution, $E(\boldsymbol{k})$ is the eigenvalue of the electron $\boldsymbol{k}$, $\boldsymbol{q}$ refers to the Fourier component of a generic perturbation, and $I(\boldsymbol{k}, \boldsymbol{q})$ is the exchange integral [often $I(\boldsymbol{k}, \boldsymbol{q})$, very difficult to calculate in real cases, is approximated to a constant]. The maxima of $J(\boldsymbol{q})$ determine a periodic magnetic moment arrangement with propagation vector $\boldsymbol{q}$.

Although the precise $J(\boldsymbol{q})$ vs $\boldsymbol{q}$ relation can only be obtained by an *ab initio* calculation involving all the bands and the appropriate matrix elements,[10] one may argue that a relevant contribution to Eq. (1) is determined by the occurrence of some parallel sheets of the FS, a well known phenomenon denoted as FS nesting. In this case, the denominator of Eq. (1) is zero for the $\boldsymbol{k}$ states pertaining to the parallel FS sheets linked by the vector $\boldsymbol{q}$, since they share the same energy, E_F, and vanishingly small for the nearby states. Although for states at the FS also the numerator of Eq. (1) is zero, the occupation of $\boldsymbol{k}$ and $(\boldsymbol{k}+\boldsymbol{q})$ states nearby the FS may be 1 and 0, respectively (or viceversa), for appropriate FS topologies (such as the one depicted in Fig. 1). In this case, $J(\boldsymbol{q})$ is very high and favors the perturbation with wave vector $\boldsymbol{q}$.

The FS nesting belongs to a class of mechanisms, all depending on the shape and the size of the FS, which have been invoked to explain a variety of phenomena, such as the spin or charge density waves (SDW, CDW), the Kohn anomalies, the Friedel oscillations, the RKKY oscillations in magnetic impurities and the oscillatory coupling in metallic magnetic multilayers. The wave vector of the perturbation would refer, in turn, to the propagation vector of the SDW or CDW, to a phonon, to an external potential, to a magnetic impurity, or to one electron itself. The archetype example of link between FS nesting and incommensurate antiferromagnetism is probably the case of chromium-based alloys.[11,12] However, it is worth realizing the qualitative difference between antiferromagnetism in chromium, where the magnetic moments are associated with the conduction electrons themselves, and in rare earths, where the magnetic moments are associated with the 4f-electrons which are not regarded as conduction electrons.

The $TmGa_3$ and $ErGa_3$ systems show different magnetic structures. $TmGa_3$ has a multiaxial, triple-$\boldsymbol{q}$ structure with propagation vectors $\boldsymbol{q}$ arising from the [1/2, 1/2, 0] star. This commensurate (but noncollinear) spin arrangement is stabilized by antiferroquadrupolar interactions, leading to an antiferroquadrupolar ordering at $T_Q=4.29$ K, located just above the Neel temperature $T_N=4.26$ K.[1–3,13] The 2D-ACAR measurements of $TmGa_3$ proposed a correlation between commensurate antiferromagnetic structures and nest-

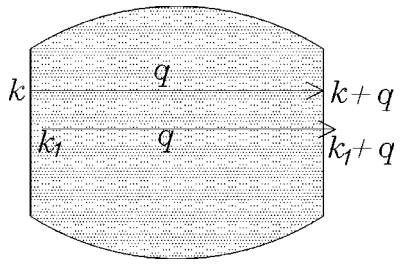

FIG. 1. Schematic example of FS nesting. The shaded region represents occupied states. Two parallel sections of the FS are highlighted by state labels $\boldsymbol{k}$ and $\boldsymbol{k}+\boldsymbol{q}$. The spanning vector $\boldsymbol{q}$ links an occupied $\boldsymbol{k_1}$ state with an unoccupied $\boldsymbol{k_1}+\boldsymbol{q}$ state. Both states have energies near to E_F.

ing of the FS along the [110]-type directions.[6] On the other hand, $ErGa_3$ orders antiferromagnetically at $T_N = 2.8$ K within an incommensurate magnetic structure. The first neutron diffraction studies, performed by Morin *et al.*[1,2] on a powder sample, yielded the propagation vector $\boldsymbol{q_a} = 2\pi/a[1/2-\delta_a, 1/2-\delta_a, 0]$, with $\delta_a = 0.020 \pm 0.003$. Further studies performed by Murasik *et al.*[14,15] on a powder sample as well as on a single crystal proposed a slightly different propagation vector $\boldsymbol{q_b} = 2\pi/a[1/2+\delta_b, 1/2, 0]$, with $\delta_b = 0.042$. In this structure the successive antiparallel (110) sheets of spins have additionally superimposed on them a sinusoidal modulation parallel to the [100] axis. One can wonder whether the incommensurate antiferromagnetism of $ErGa_3$ can be linked to an appropriate FS topology as well.

Previous dHvA experiments, providing only evaluations of the *extremal cross sectional areas* of the FS perpendicular to an applied magnetic field, could not investigate the nesting properties of the FS. Conversely, the 2D-ACAR technique has the unique ability to sample the Brillouin zone (BZ) of truly three-dimensional systems in a cartesian mesh and unveil nesting features of the FS.[6,16,17]

In detail, by measuring the distribution $N(\theta_x, \theta_y)$ of the deviation angles from anticollinearity of the annihilation γ rays, the experiment determines a two-dimensional (2D) projection of the 3D electron–positron (ep) momentum density, $\rho^{\mathrm{ep}}(\boldsymbol{p})$.[18,19] The contribution to $\rho^{\mathrm{ep}}(\boldsymbol{p})$ from the conduction bands l is discontinuous at points $\boldsymbol{p}_{F_l} = (\boldsymbol{k}_{F_l} + \boldsymbol{G})$, where $\boldsymbol{G}$ is a reciprocal lattice vector and $\boldsymbol{k}_{F_l}$ are the reduced Fermi wave vectors in the first Brillouin zone. The standard Lock–Crisp–West (LCW) transformation,[20] extensively used in the data analysis of the 2D-ACAR spectra, reinforces these discontinuities by folding the momentum distribution $\rho^{\mathrm{ep}}(\boldsymbol{p})$ back onto the first BZ by translation over the appropriate vectors $\boldsymbol{G}$. If the summation is performed over a sufficient portion of momentum space the result is,[21]

$$\rho^{\mathrm{ep}}_{\mathrm{LCW}}(\boldsymbol{k}) = \sum_n \theta(E_F - \epsilon_{\boldsymbol{k},n}) \int |\psi^n_{\boldsymbol{k}}(\boldsymbol{r})|^2 \, |\phi(\boldsymbol{r})|^2 \, g^n_{\boldsymbol{k}}(\boldsymbol{r}) d\boldsymbol{r}. \tag{2}$$

Here ϕ denotes the positron wave function, $\epsilon_{\boldsymbol{k},n}$ is the energy eigenvalue of the electron from band n with Bloch wave vector $\boldsymbol{k}$, and wave function $\psi^n_{\boldsymbol{k}}$. The factor $g^n_{\boldsymbol{k}}(\boldsymbol{r})$ accounts for the ep correlations.[22,23] In general, although the mapping of the FS is facilitated when the overlap integral in Eq. (2) is a weakly varying function of $\boldsymbol{k}$, the FS discontinuities [marked by the step function of Eq. (2)] are not shifted by this $\boldsymbol{k}$-dependence.[24] In practice, prior to applying the 3D LCW transformation it is necessary to reconstruct tomographically the 3D $\rho^{\mathrm{ep}}(\boldsymbol{p})$ on the base of its 2D projections.

In this work, we provide a topological description of the FS sheets of $ErGa_3$. The results are compared to dHvA experiments and LMTO calculations on $ErGa_3$ (Ref. 4) and to the previous 2D-ACAR experiments on $TmGa_3$.[6] Further information is obtained complementing the LMTO results with *ab initio* band structure calculations produced by the code WIEN97,[25] adopting the full potential linearised augmented plane wave (FLAPW) method within the LDA. Finally, we analyze in detail the nesting properties of the FS of $ErGa_3$ and discuss their consistency with the magnetic structure of this system.

II. EXPERIMENTAL PROCEDURES AND DETAILS OF THE CALCULATIONS

The crystal structure of $ErGa_3$ and $TmGa_3$ is the cubic $L1_2$ (space group *Pm3m*), with lattice constants $a = 4.212$ Å and $a = 4.196$ Å for $ErGa_3$ and $TmGa_3$, respectively. The $ErGa_3$ single crystals were grown by the molten-metal solution method. The melt, of composition 90 at % Ga and 10 at % Er, was cooled at the slow rate of 0.8 °C/h from 900 °C to 280 °C and then brought rapidly down to room temperature to avoid $ErGa_6$ formation. The purities of the substrates were 4N and 6N for Er and Ga, respectively. This procedure yielded single crystals of stoichiometric composition immersed in an excess of pure gallium which could easily be removed. An x-ray diffraction experiment, using the von Laue technique in back reflection, confirmed the final single crystalline state. The 2D-ACAR experiments were carried out in the paramagnetic phase with a set-up based on a pair of Anger cameras, described in detail in Ref. 26. Four projections were collected, with integration directions (perpendicular to $\boldsymbol{p}_z \equiv [001]$ axis) at $0° \equiv [100]$, 15°, 30°, and $45° \equiv [110]$. Each spectrum, acquired at the temperature of 60 K in a vacuum of 1×10^{-6} Torr, accumulated $\approx 3 \times 10^8$ raw coincidence counts in a (288×288) matrix with a bin size of (0.02×0.02) a.u.^{2} The estimated overall experimental resolution, obtained by combining the intrinsic angular resolution with the intrinsic sizes of the positron-source spot at the sample and the thermal motion of the positron (~ 0.03 a.u., at 60 K), was (0.08,0.13) a.u. at 60 K for the p_z and p_y directions, equivalent to 10% and 17% of the BZ size, respectively. The spectra were subjected to the usual correction procedure, which removes the distortions resulting from spatial variations in the single detector efficiencies and the finite apertures of those detectors,[27] and aligned to the ideal center of the matrix via mechanical translation of the whole source-sample assembly along the horizontal and vertical direction. Next, after applying the Van Citter–Gerhardt deconvolution algorithm,[28] the electron–positron momentum densities $\rho^{\mathrm{ep}}(\boldsymbol{p})$ were reconstructed (on planes perpendicular to the main symmetry axis, $\boldsymbol{p}_z \equiv [001]$) by Cormack's[29] and modified filtered-back-projection (FBP) (Ref. 30) algorithms. Unlike the typical medical imaging reconstruction techniques, both methods exploit the crystal symmetry and can provide a faithful reconstruction of $\rho^{\mathrm{ep}}(\boldsymbol{p})$ from a small number of projections depending on the amount of its anisotropy.[30] In this case four projections proved to be adequate. A detailed description of both methods will appear in Ref. 31. Finally, the 3D-LCW (Ref. 20) transformation was applied. Since, as mentioned above, the reconstruction of the 3D density $\rho^{\mathrm{ep}}(p_x, p_y, p_z)$ was reduced to a set of reconstructions of independent 2D densities piled up along the [001] direction, the resulting irreducible wedge of the BZ (W_{BZ}) had the symmetry of a tetragonal BZ ($W_{\mathrm{BZ}} = 1/16$ BZ). Therefore, after examining that the LCW density did reflect the cubic symmetry, the condition,

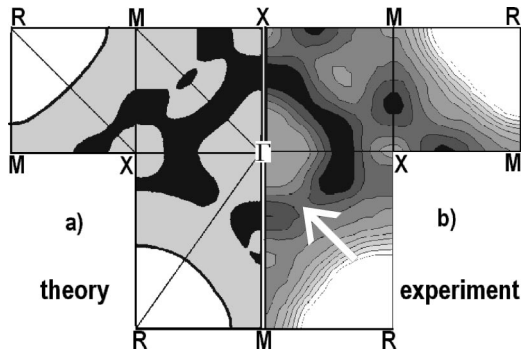

FIG. 2. (a) Sections of the calculated FS of paramagnetic $ErGa_3$ in high symmetry plane of the BZ. The white region centered at the R points includes the occupied states of band 7 and the black region includes the unoccupied states of band 6 (from Ref. 5). (b) Experimental $\rho^{ep}_{LCW}(\boldsymbol{k})$ along the same symmetry planes as (a). The arrow highlights the increase in the occupancy along ΓR discussed in the text. The labeling indicates the high symmetry points of the BZ.

$$\rho^{ep}_{LCW}(k_x,k_y,k_z)=\rho^{ep}_{LCW}(k_y,k_z,k_x)=\rho^{ep}_{LCW}(k_x,k_z,k_y) \tag{3}$$

was enforced. The application of Eq. (3) restored the full cubic symmetry ($W_{BZ}=1/48$ BZ) and improved the statistics of the LCW density.

The total amplitude variation of the resulting 3D-LCW densities provided by both reconstruction methods (Cormack, FBP) was 18%. Since the overall features of the two LCW densities were extremely similar, apart from a higher contribution from the noise in the FBP case, only Cormack's results will be shown next.[32]

The band structure was calculated using the self-consistent FLAPW method[25] within the LDA. The experimental lattice parameters reported above were utilized. In the interstitial region, the plane waves expansion was truncated at the maximum wave vector $K_{max}=3.1$ a.u. Inside the muffin tin spheres we used spherical harmonics with angular momenta up to $l_{max}=10$ for the potential, the charge density and the wave functions. The *f-core* model was accomplished by forcing an Er $4f^{11}$ core configuration. The energy parameter for the 4f orbitals was set at very high value (~2 Ry) thus excluding the Er *f* component from the valence states. The self-consistent calculation was performed including spin orbit coupling at each variational step, as suggested in Ref. 5.

The irreducible BZ was sampled using 165 special *k*-points according to the linear tetrahedra method. The muffin tin radius was R=2.6 a.u. for Er and Ga, respectively.

III. RESULTS AND DISCUSSIONS

We start our discussion by showing in Fig. 2(a) the intersections of the FS resulting from the *f-core* LMTO calculation[5] with the high symmetry planes of the cubic BZ. The electronlike part of the FS (following Ref. 5 we label the corresponding conduction band by number 7) is a simple spheroidal pocket centered at the R points. Conversely, the holelike part of the FS (from band 6) is a complicated, multiply-connected, structure surrounding the X points and the Γ point. Since $ErGa_3$ is a compensated metal, the volume enclosed by the electronlike FS equals that of the holelike. Figure 2(b) shows slices of $\rho^{ep}_{LCW}(\boldsymbol{k})$ along the same symmetry planes of the BZ as Fig. 2(a). The broad maxima in the regions centered at the R points of the BZ are in good agreement with the electronlike spheroidal FS (from band 7) predicted by the theory [see Fig. 2(a)].

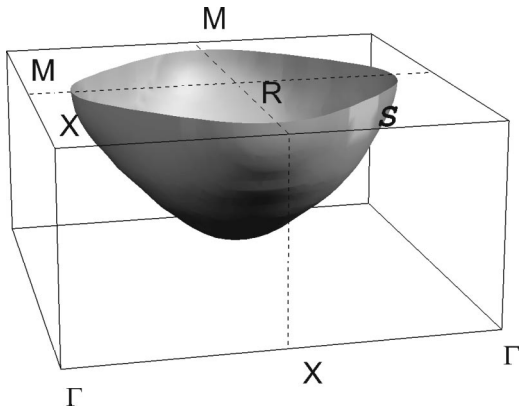

FIG. 3. Experimental electron part of the FS for $ErGa_3$, shown in half BZ after shifting the R point at the center of the BZ. The nesting part of the FS (see text) is denoted by letter S.

Figure 3 shows a 3D view of the isodensity surface, identified as FS, selected at the loci of the largest amplitude variation of $\rho^{ep}_{LCW}(\boldsymbol{k})$ (the FS is shown after shifting the corner of the BZ to the center of the BZ). To select the appropriate value of the LCW density we have devised the following procedure: the whole amplitude variation of $\rho^{ep}_{LCW}(\boldsymbol{k})$ is scanned at values Δ^i, keeping the step $\delta\Delta=\Delta^i-\Delta^{i-1}$ constant. For each value Δ^i we calculate the area $A(\Delta^i)$ of the isodensity surface, $\rho^{ep}_{LCW}(\boldsymbol{k})=\Delta^i$, and the volume $(\Delta V)^i$ included between the isodensity surfaces $\rho^{ep}_{LCW}(\boldsymbol{k})=\Delta^i$ and $\rho^{ep}_{LCW}(\boldsymbol{k})=\Delta^{i-1}$ (the surfaces are approximated by several polygons[33]). Then, the ratio $(\Delta V)^i/A(\Delta^i)$ provides an average $|\delta k^i|$ which can be utilized to yield an average LCW density gradient $|\delta\Delta/\delta k^i|$.

The maxima of the average gradient plotted against the LCW densities Δ^i, shown in Fig. 4, provide the LCW density values of the highest amplitude variations, Δ_{M_i}, and the related isodensity surfaces $\rho^{ep}_{LCW}(\boldsymbol{k})=\Delta_{M_i}$ establish our

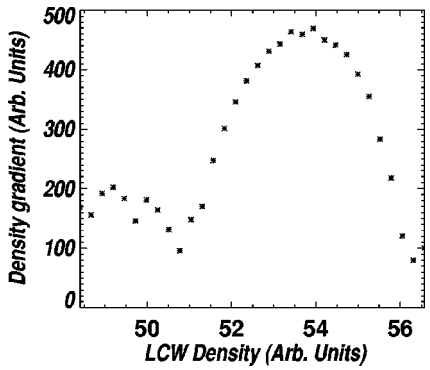

FIG. 4. Plot of the gradient of $\rho^{ep}_{LCW}(\boldsymbol{k})$ vs the LCW density for $ErGa_3$ according to the procedure discussed in the text.

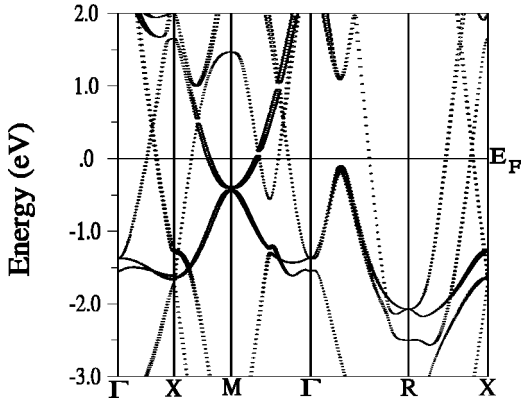

FIG. 5. The energy bands of $ErGa_3$ calculated with a self-consistent FLAPW calculation along high symmetry directions of the BZ. All the energies are referred to the Fermi level, and set to zero. The symbol size is set to be proportional to the *d* orbital character inside the Er sphere.

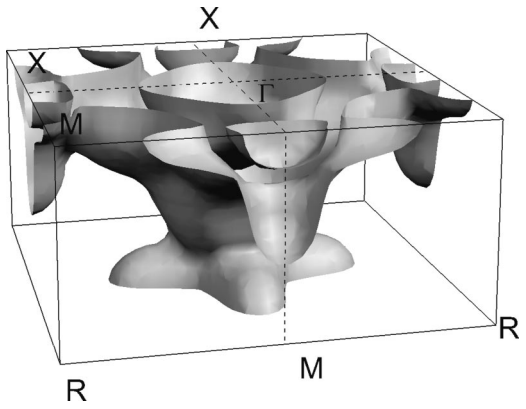

FIG. 6. Experimental holelike part of the FS for $ErGa_3$, shown in half BZ. The unoccupied region lies between the inner surface, centered at Γ and X, and the outer surface.

guesses of the Fermi surface. The large maximum of Fig. 4, at the LCW density ~ 54 [very near to the value of $\rho^{\mathrm{ep}}_{\mathrm{LCW}}(\boldsymbol{k})$ at $k \sim \overline{XR}/2$ in Fig. 2(b)] addresses the FS sheet shown in Fig. 3.

The further structure in the regions surrounding the Γ and X points in Fig. 2(b) is similar to the occupancy of the theoretical holelike Fermi volume from band 6 shown in Fig. 2(a). Nevertheless, Fig. 4 does not show clearly a local maximum of the gradient $|\delta\Delta/\delta k^i|$, defining a threshold for the holelike FS. One can investigate the reason of this difference by looking at the orbital character (s,p,d) of the $\boldsymbol{k}$ states calculated by the code WIEN97. To this end, Fig. 5 shows the band structure of $ErGa_3$ along the high symmetry directions of the cubic BZ [the energy bands are in good agreement with those of the LMTO calculation (Ref. 4)].

Furthermore, in Fig. 5 the size of the symbol representative of the energy values is set to be proportional to the *d* orbital character of the $\boldsymbol{k}$ state inside the Er sphere. It appears that band 6, generating the holelike FS shown in Fig. 2(a), shows a substantial Er-*d* character around the M point (due to the t_{2g} orbitals) and, to a minor extent, along ΓX. Since the *d* features increase the localization of the $\boldsymbol{k}$ states at the expenses of their overlap with the positron, which resides prevalently in the interstices, the discontinuities of $\rho^{\mathrm{ep}}_{\mathrm{LCW}}(\boldsymbol{k})$ across the pertaining $\boldsymbol{k}_{F_l}$ points are reduced [see Eq. (2)].

Conversely, band 7, centered at the R point and originating the FS sheet shown in Fig. 3, has very little Er-*d* character. Therefore, higher delocalization of the related $\boldsymbol{k}$ states and a higher overlap with the positron density should be expected. The higher dispersion of band 7 with respect to band 6 reinforces this conjecture [at the corresponding k_F points the calculation[25] yields average gradients of $|\nabla\epsilon(k)| \simeq 18$ eV/a.u. and $|\nabla\epsilon(k)| \simeq 10$ eV/a.u. for band 7 and 6, respectively].

A further reason for a smaller amplitude variation due to the Fermi breaks of band 6 with respect to those of band 7 (generating a simple, convex FS) is due to their proximity. As shown in Fig. 5, for all symmetry directions, but particularly along ΓX, MΓ, and RX, the Fermi breaks of band 6 are located in pairs, with a distance between the breaks comparable with the experimental resolution. Consequently, the amplitude variation generated by the convolution of these discontinuity-pairs with the experimental resolution is reduced.[34]

In view of the uncertainty concerning the position of the Fermi edge of the holelike FS, we selected the isodensity surface which yielded the closest volume to the electronlike part of the FS. The Fermi volumes obtained, corresponding to $(19\pm2)\%$ and $(23\pm5)\%$ of the BZ for the electronlike FS and the holelike FS, respectively, are equivalent to 0.38 electrons and 0.46 holes per formula units, assuming spin degeneracy. These figures are in good agreement with those obtained by the FLAPW calculation, yielding 18% of the BZ volume for the electronlike and holelike FSs. Figure 6 shows the multiply connected topology attributed to the holelike FS. The major discrepancy with the theory[5,25] consists of the absence of the interruption of the FS in the ΓR direction [see Fig. 2(a), where, on going from Γ to R, only the Fermi edge due to band 7 is found, unlike the experimental case shown in Fig. 2(b)]. However, since Fig. 2(b) shows that the intensity of $\rho^{\mathrm{ep}}_{\mathrm{LCW}}(\boldsymbol{k})$ along ΓR at the point highlighted by the arrow is higher than that at the nearby points, one can explain the discrepancy as simply due to insufficient instrumental resolution.

Our estimates of the FS sizes can be compared to the dHvA experiment. Table I reports the extremal cross sectional areas perpendicular to high symmetry directions of the BZ, expressed as dHvA frequencies, and the corresponding dHvA measured frequencies. The comparison should also elucidate the experimental error in our determination of the FS due to (i) the uncertainty in the choice of the isodensity surface; (ii) the fact that identifying the FS with an isodensity surface implies that the overlap integral in Eq. (2) is constant for the $\boldsymbol{k}$ states at the FS of a single band.

Table I shows that the agreement with the dHvA experiments is particularly satisfactory for the dHvA branch labeled by (a). This branch is generated by the electronlike FS, which as described above, was determined with higher accuracy.

Although the good agreement with the dHvA experiment,

TABLE I. 2D-ACAR experimental extremal cross sectional areas of the FS normal to high symmetry direction of the BZ, expressed as dHvA frequencies, compared to the frequencies detected by the dHvA experiment (Ref. 5) (the letters in parentheses refer to the dHvA branches in Fig. 5 of Ref. 5).

[100] F (10^6 G)		[110] F (10^6 G)		[111] F (10^6 G)	
2D-ACAR	dHvA	2D-ACAR	dHvA	2D-ACAR	dHvA
101 ± 2	98 (a)	95 ± 2	96 (a)	91 ± 2	88 (a)
40 ± 2	41 (d)				35 (d)
35 ± 2	30 (d')	37 ± 2		32 ± 2	
9 ± 2	13 (b)	11 ± 2	12 (b)	11 ± 2	

supporting to a fair extent the *f*-core model, can be considered an interesting result, it is the direct access to the topology of the FS and the investigation of its nesting properties which makes our experiment a rather unique tool. Indeed, a significant part of the electronlike FS (see Fig. 3, nearby letter S, and Fig. 7) does show nesting features in the [110] directions. Figure 7(a), shows in a repeated zone scheme the sections of the FS in the $k_z=\pi/a$ plane of the BZ and the relevant spanning vectors $\boldsymbol{q_1}$ and $\boldsymbol{q_2}$. Figure 7(b) shows that the nesting feature persists along the [001] direction for $\simeq 0.2$ a.u., to yield a total nesting area of $\simeq 0.06$ a.u.^{2}, equivalent to 9% of $(2\pi/a)^2$.

Unlike the archetype case of chromium, where the nesting occurs between different sheets of the FS, we notice here that

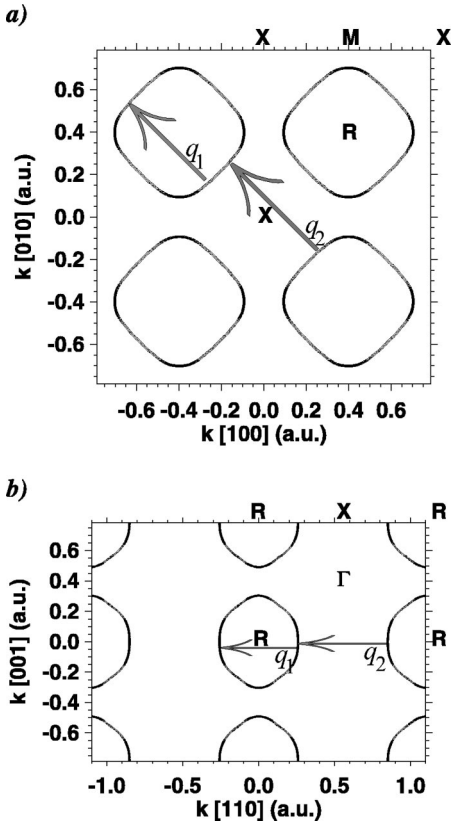

FIG. 7. (a) Intersections of the electronlike FS, in a repeated zone scheme, with the plane $k_z=\pi/a$. The two spanning vectors, q_1 and q_2 connect the parallel sections of the FS. (b) Same as (a) for a (110) plane of the BZ.

one FS sheet is nesting into itself. This behavior was predicted in other rare earth systems and linked to the magnetic structure observed.[35]

The soundness of the nesting features is highlighted by the thickness of the contour line, corresponding to a range of $\rho^{\mathrm{ep}}_{\mathrm{LCW}}(\boldsymbol{k})$ within 5% of its total amplitude variation. This means that a slightly different choice in the isodensity surface defining the FS neither effects sensibly the shape of the FS sections nor the length of the spanning vectors. We also tested the stability of the nesting feature against numerical noise. To do so, additional Poissonian noise was applied to the four raw 2D projections and its propagation through the 3D reconstruction (Cormack's method) and 3D LCW folding was investigated. Remarkably, the consequent LCW density (not shown) displayed very similar nesting features.

The vectors $\boldsymbol{q_1}$ and $\boldsymbol{q_2}$ can be expressed in terms of the lattice commensurate spanning vector $\boldsymbol{q_c}=2\pi/a[1/2,1/2,0]$ as $\boldsymbol{q_1}=\boldsymbol{q_c}(1-\delta)$ and $\boldsymbol{q_2}=\boldsymbol{q_c}(1+\delta)$, with $\delta=(0.03\pm0.01)$ [the LCW density obtained via the FBP reconstruction method yields $\delta=(0.025\pm0.010)$]. The equivalence of the two vectors is revealed by summing to $\boldsymbol{q_2}$ the reciprocal lattice vector $\boldsymbol{G_1}=-2\pi/a[1,1,0]$, to yield $\boldsymbol{q_{2'}}=\boldsymbol{q_2}+\boldsymbol{G_1}=-\boldsymbol{q_1}$. In principle,[11,12] the vectors $\boldsymbol{q_1}$ and $-\boldsymbol{q_1}$ would single out helical waves with positive and negative helicity which combine to produce a linearly polarized sinusoidal spin modulation with period $\lambda_m=2\pi/\delta$, modulating the commensurate antiferromagnetic wave along the [110] direction. It is worth noticing that, among the variety of periodic magnetic arrangements commonly observed in lanthanides systems, such as ferromagnetic, helical antiferromagnetic, conical antiferromagnetic, and sinusoidal antiferromagnetic, the latter was detected in $ErGa_3$ by the neutron diffraction experiments.[1,14]

The periodicity λ_m corresponds to $\simeq 33$ times the interplanar distance in the [110] direction ($\lambda_m\simeq 100$ Å). The parameter δ is consistent with the incommensurability parameter $\delta_1=(0.020\pm0.003)$ found by the neutron diffraction experiments of Morin *et al.*[1] Nevertheless, one can object that the agreement between δ and the values obtained from the neutron experiments is not relevant since the difference between $\boldsymbol{q_1}$ and $\boldsymbol{q_c}$ is only ~ 3 times its statistical uncertainty. Indeed, by lowering appropriately the selected LCW density value (about 10% of the total amplitude variation) the resulting spanning vectors $\boldsymbol{q_1}$ and $\boldsymbol{q_2}$ coincide with $\boldsymbol{q_c}$, reflecting a commensurate antiferromagnetism. However, this action, yielding larger sections of the R-centered spheroidal FS, has

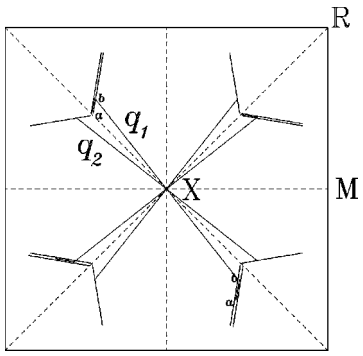

FIG. 8. Schematic example of one possible FS nesting consistent with the neutron scattering experiments of Murasik *et al.* (Ref. 14) and the cubic symmetry. The spanning vectors $\boldsymbol{q_1}$ and $\boldsymbol{q_2}$, linking the parallel FS sections labeled by letters *a*–*b*, address the incommensurate modulation described in the text. The labeling in capital letters indicates the high symmetry points of the BZ as in Fig. 7 (the departure of $\boldsymbol{q_1}$ and $\boldsymbol{q_2}$ from the direction [110] is exaggerated in the figure).

the effect to increase the calculated dHvA frequencies reported in the first line of Table I by $\simeq 10\%$, with a departure from the experimental dHvA values of branch (a).

On the other hand, as already mentioned, the recent and more complete measurements of Murasik *et al.*[14] have proposed a somewhat different propagation vector $\boldsymbol{q_b} = 2\pi/a[1/2+\delta_b,1/2,0]$, with $\delta_b = 0.042$. The authors explain their results in terms of adjacent antiparallel (110) sheets of spins superimposed onto a sinusoidal modulation parallel to the [100] axis.

In principle, the FS topology might reflect this periodic arrangement with the presence of parallel sheets having different orientation with respect to the (110) planes, as shown in the schematic example of Fig. 8. However, for a state of the art 2D-ACAR experiment it would be difficult to appraise the slight change in the shape of the FS (exaggerated in Fig. 8) required to agree with the incommensurability parameter suggested by Murasik *et al.*[14] Nevertheless, we can investigate further the electronic structure of $ErGa_3$ by comparing its LCW density $\rho^{ep}_{LCW}(\boldsymbol{k})$ with the corresponding one obtained for $TmGa_3$, where an FS driven commensurate antiferromagnetism was suggested.[6] Figure 9 shows the LCW densities of $ErGa_3$ and $TmGa_3$ along the two high symmetry planes of the BZ, $k_z = \pi/a$ [Fig. 9(I)] and $k_z = 0$ [Fig. 9(II)]. Although the two LCW densities are rather similar, the shape of the contour lines does show clear differences. In particular, the nesting addressed by the flat part of the contour lines of Fig. 9(I) for $ErGa_3$, marked by the arrow, is much less evident for $TmGa_3$. Conversely, Fig. 9(II) shows flat (i.e., nesting) contour lines for $TmGa_3$ (see arrow and check Ref. 6), consistent with a commensurate antiferromagnetism, which do not appear in $ErGa_3$.

Furthermore, we notice that several sections of the holelike FS sheet of $ErGa_3$ show nesting features along the [100] direction. Figure 10 displays intersections of the holelike FS with planes of the BZ parallel to the $k_z = 0$ plane and laying in between the XMR and the ΓXM planes. For better comparison, the intersections have been translated onto the same

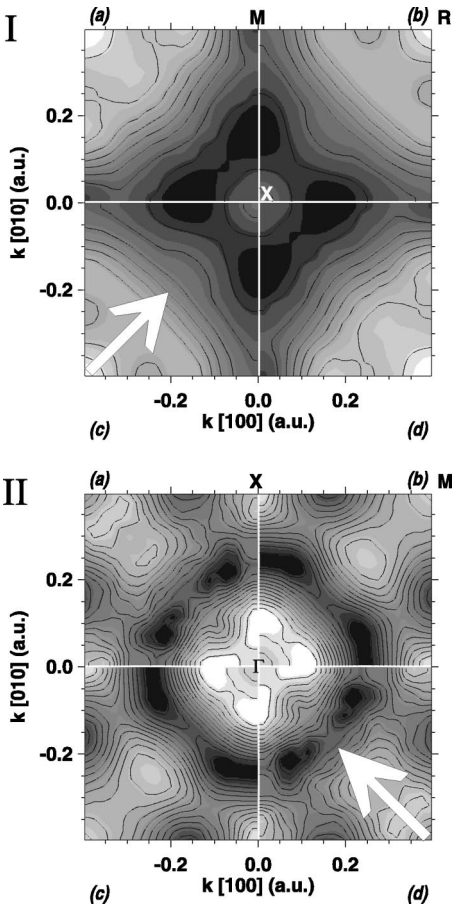

FIG. 9. **I**. LCW densities of $ErGa_3$ [quadrants (b) and (c)] and $TmGa_3$ [quadrants (a) and (d)] in the $k_z = \pi/a$ plane of the BZ. The arrow highlights the nesting feature attributed to $ErGa_3$ (see text). **II**. LCW densities of $ErGa_3$ [quadrants (b) and (c)] and $TmGa_3$ [quadrants (a) and (d)] in the $k_z = 0$ plane of the BZ. The arrow highlights the nesting feature attributed to $TmGa_3$ in Ref. 6.

plane. It appears that the intersections in the region between ~ 0.1 a.u. and ~ 0.15 a.u. from the origin (0,0) are approximately parallel to the [100]-type directions. These features of the FS are missing in the case of $TmGa_3$. A careful analysis

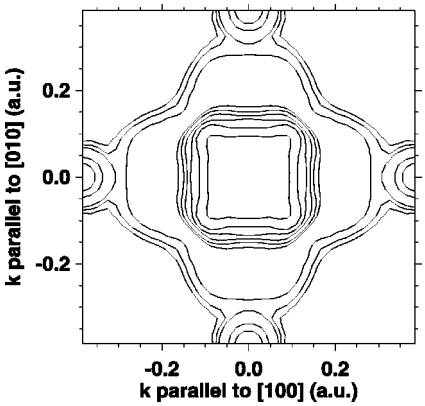

FIG. 10. Intersections of the holelike FS of $ErGa_3$ with several planes of the BZ parallel to the $k_z = 0$ plane, after being projected on the $k_z = 0$ plane itself.

has established that the differences in the FS topologies of the two compounds cannot be ascribed to details of the reconstruction algorithm input. Therefore, it is tempting to link the topology of the FSs with the magnetic structures of the two systems.

We completed our analysis extracting from the two FS sheets obtained for $ErGa_3$ estimates of the electronic density of states (DOS) at the Fermi energy, $N(E_F)$, and the electronic part of the specific heat (per unit temperature) γ.

As described in Ref. 6, our method is based on the definition of $N(E_F)$,

$$N(E_F)=\frac{1}{4\pi^3}\int_S \frac{dS}{|\nabla_k \epsilon|}, \tag{4}$$

where the integral is over the FS, experimentally available, and the gradient of the energy function at $\boldsymbol{k}_F$, $\nabla_k \epsilon$, is obtained from our band structure calculation (see values reported above for the two conduction bands). The γ values obtained, $\gamma \simeq (0.49 \pm 0.04)$ mJ/(mol K^2) and $\gamma \simeq (2.2 \pm 0.4)$ mJ/(mol K^2) for the electronlike and holelike FSs, respectively, cannot be compared to the experimental calorimetric values of γ because of the strong magnetic contribution to the specific heat yielded by the near magnetic transition ($T_N = 2.8$ K). Nevertheless, the overall $\gamma \simeq (2.7 \pm 0.4)$ mJ/(mol K^2), corresponding to a density of states $N(E_F)=(16\pm 2)$ states/(Ryd cell) is not far from what obtained by the LMTO calculation,[5] $N(E_F)=22.5$ states/(Ryd cell, Ref. 36), and by our f-core FLAPW calculation [$N(E_F)=25$ states/(Ryd cell)].

IV. CONCLUSIONS

The measurement of the angular correlation of the ep annihilation radiation in a single crystal of $ErGa_3$ has been utilized to reconstruct the 3D ep momentum density and obtain information on the topology of the FS. Two FS sheets have been suggested, in fair agreement with the prediction of the *f-core* LDA theory. The electronlike FS, determined with higher accuracy, displays a clear nesting feature, with a spanning vector $\boldsymbol{q_1}$ in the [110]-type directions, consistent with the overall magnetic structure of the system. A further nesting feature of the holelike FS is observed in the [100]-type directions. Although neutron scattering experiments detect only one propagation vector in $ErGa_3$ (magnetic structure of $\boldsymbol{k_1}$ type) one may argue that the nesting along the [100]-type directions is related to the incommensurate moment modulation observed along [100].[14]

These findings are different from those obtained for the isostructural $4f^{12}$ system $TmGa_3$, where our previous 2D-ACAR measurements suggested a FS nesting commensurate with the lattice.[6] A natural explanation for the differences in the FSs proposed in this work is that the band structure actually does change from one compound ($ErGa_3$) to the other ($TmGa_3$) when proceeding along the rare earth series. Small differences in the FS (incompatible with the standard, *f*-band, LDA band structure calculations) were detected in the RE-B_6 (RE=La, Ce, Pr, Nd) systems as well.[37] Obviously, such changes cannot be predicted by an *f*-core LDA calculation, considering the RE atoms at stake, only the $5d^1$ and $6s^2$ electrons are itinerant. Few speculations on the nature of these differences can be proposed. Within the f-core model, one can suggest that the polarization of the conduction electrons due to their coupling with the f-electrons could lead to modifications of the band structure. In this regard, inelastic neutron scattering experiments have established that, owing to crystal field splitting, the ground states of the f multiplets are the Γ_7 doublet and the $\Gamma_5^{(1)}$ triplet for $ErGa_3$ and $TmGa_3$, respectively.[1,2,38] The occurrence of a quadrupolar moment associated with the $\Gamma_5^{(1)}$ ground state of $TmGa_3$, absent in $ErGa_3$, may produce the aforementioned differences in the band structure.

On the other hand, one may infer that the band structure changes due to hybridization with the 4f states. Since there is strong evidence that the standard LDA tends to overestimate the hybridization, leading to FSs in strong contrast with the experiments, other methods should be employed to describe appropriately a small hybridization of the $4f$ electrons with the conduction electrons. Among alternative *semi ab initio* calculations, it is worth recalling the self-interaction correction, known to increase the localization of the one-electron spatial wave functions,[39] the ''LDA+U'' method, which aims at accounting for the strong on-site atomiclike correlation effects of the $4f$ electrons,[40] or the dynamical field theory, which adopts the single impurity Anderson model imbedded in an effective medium determined self-consistently.[41] In this regard, the subtle differences revealed in the FS topologies of $ErGa_3$ and $TmGa_3$ may provide useful insights to test the various theoretical approaches.

ACKNOWLEDGMENTS

We thank Professor E. Bruno and Dr. M. Wolcyrz for stimulating discussions.

*Also at Istituto Nazionale di Fisica della Materia.

†Author to whom correspondence should be addressed. Electronic address: Biasini@bologna.enea.it

[1] P. Morin, M. Giraud, P.L. Regnault, E. Roudaut, and A. Czopnik, J. Magn. Magn. Mater. **66**, 345 (1987).

[2] P. Morin, M. Giraud, P. Burlet, and A. Czopnik, J. Magn. Magn. Mater. **68**, 107 (1987).

[3] P. Morin, P. Rouchy, M. Giraud, and A. Czopnik, J. Magn. Magn. Mater. **67**, 95 (1987).

[4] V.B. Pluzhnikov, A. Czopnik, G.E. Grechnev, N.V. Savchenko, and W. Suski, Phys. Rev. B **59**, 7893 (1999).

[5] V.B. Pluzhnikov, A. Czopnik, and G.E. Grechnev, J. Phys. Condens. Matter **11**, 4507 (1999).

[6] M. Biasini, G. Kontrym-Sznajd, M.A. Monge, M. Gemmi, A. Czopnik, and A. Jura, Phys. Rev. Lett. **86**, 4612 (2001).

[7] R.W. Williams, T.L. Loucks, and A.R. Mackintosh, Phys. Rev. Lett. **16**, 168 (1966).

[8] C Kittel, *Solid State Physics*, edited by F. Seitz, D. Turnbull, and

H. Ehrensch (Academic, New York, 1968), Vol. 22, p. 1. The expression given by Kittel refers to the free electron model, to a real perturbation and a constant exchange integral.

[9] S. Legvold, in *Ferromagnetic Materials*, edited by E.P. Wohlfhart (North–Holland, Amsterdam, 1980), Vol. 1, p. 191.

[10] See, for example, D. Schmitt and P.M. Levy, J. Magn. Magn. Mater. **49**, 15 (1985); K. Schwartzman, J.L. Fry, and Y.Z. Zhao, Phys. Rev. B **40**, 454 (1989); J.B. Staunton, J. Poulter, B. Ginatempo, E. Bruno, and D.D. Johnson, Phys. Rev. Lett. **82**, 3340 (1999).

[11] A.W. Overhauser, Phys. Rev. **128**, 1437 (1962).

[12] E. Fawcett, Rev. Mod. Phys. **60**, 209 (1988).

[13] Z. Kletowski, P.J. Markowski, and A. Czopnik, Solid State Commun. **65**, 593 (1988).

[14] A. Murasik, A. Czopnik, L. Keller, and P. Fischer, J. Magn. Magn. Mater. **213**, 101 (2000).

[15] A. Murasik, A. Czopnik, L. Keller, and P. Fischer, Phys. Status Solidi A **173**, R1 (1999).

[16] It is worth mentioning that the 3D reconstruction of the FS can also be attained by Compton scattering experiments. See, for example, I. Matsumoto, H. Kawata, and N. Shiotani, Phys. Rev. B **64**, 195132 (2001). However, the double integration of the momentum density and the complex samples preparation, makes a 3D reconstruction a quite complicated task. Furthermore, nowadays also the angular resolved photoemission (ARPES) technique provides relevant information on the topology of the FS. Nevertheless, even solving the difficult problem of determining the Bloch wave vector perpendicular to the sample surface, $k_{\perp}$, ARPES can only measure the electronic occupancy in spherical shells of the BZ, as described by D. Ehm, F. Reinert, G. Nicolay, S. Schmidt, S. Huefner, R. Claessen, V. Eyert, and C. Geibel, Phys. Rev. B **64**, 235104 (2001). In practice, ARPES experiments are very effective when applied to quasi-2D systems.

[17] S.B. Dugdale, H.M. Fretwell, M.A. Alam, G. Kontrym-Sznajd, R.N. West, and S. Baldrzadeh, Phys. Rev. Lett. **79**, 941 (1997).

[18] S. Berko, *Proc. Int. School Phys. Enrico Fermi*, edited by W. Brandt and A. Dupasquier (North–Holland, Amsterdam, 1983), p. 64.

[19] R. N. West, *Proc. Int. School Phys. Enrico Fermi*, edited by A. Dupasquier and A. P. Mills Jr. (North–Holland, Amsterdam, 1993), p. 75.

[20] D.G. Lock, V.H. Crisp, and R.N. West, J. Phys. F: Met. Phys. **3**, 561 (1973).

[21] J.H. Kaiser, R.N. West, and N. Shiotani, J. Phys. F: Met. Phys. **16**, 1307 (1986).

[22] E. Boronski and R.M. Nieminen, Phys. Rev. B **34**, 3820 (1986); H. Sormann, *ibid*. **54**, 4558 1996.

[23] A. Rubaszek, Z. Szotek, and W.M. Temmermann, Phys. Rev. B **58**, 11 285 (1998).

[24] C.K. Majumdar, Phys. Rev. A **140**, 227 (1965).

[25] P. Blaha, K. Schwartz, and J. Luitz, WIEN97, A Full Potential Linearized Augmented Plane Wave Package for calculating crystal properties (Tech. Universität Wien, Austria, 1999).

[26] M. Biasini, G. Ferro, M. Monge, G. di Francia, and V. La Ferrara, J. Phys. Condens. Matter **12**, 5961 (2000).

[27] R.N. West, J. Mayers, and P.A. Walters, J. Phys. E **14**, 478 (1979).

[28] U. Gerhardt, S. Marquardt, N. Schroeder, and S. Weiss, Phys. Rev. B **58**, 6877 (1998).

[29] A.M. Cormack, J. Appl. Phys. **35**, 2908 (1964).

[30] G. Kontrym-Sznajd and E. Jozefczuk, Mater. Sci. Forum **255-257**, 754 (1997).

[31] G. Kontrym-Sznajd *et al.* (to be published).

[32] The lower statistical noise of Cormack's method is due to the expansion of the experimental data into orthogonal polynomials.

[33] A. Lorenson and P. Cline, Comput. Graphics **21**, 163 (1987).

[34] Obviously, our deconvolution routine cannot tackle fully this problem. Indeed, a particularly severe obstacle for any deconvolution algorithm exists when the original (true) data contain first order discontinuities, such as the Fermi breakes, characterized (intrinsically) by low *numerical* entropy.

[35] O. Krogh Andersen and T.L. Loucks, Phys. Rev. **167**, 551 (1968).

[36] G.E. Grechnev (private communication).

[37] Y. Onuki, T. Komatsubara, P.H.P. Reinders, and M. Springford, J. Phys. Soc. Jpn. **58**, 3698 (1989); Y. Onuki, A. Umezawa, K. Kwok, G.W. Crabtree, N. Nishihara, T. Yamazaki, T. Omi, and T. Komatsubara, Phys. Rev. B **40**, 11 195 (1989); Y. Kubo and S. Asano, J. Magn. Magn. Mater. **104**, 1182 (1992).

[38] A. Murasik, A. Czopnik, E. Clementyev, and J. Schefer, J. Magn. Magn. Mater. **222**, 101 (2000).

[39] J.P. Perdew and A. Zunger, Phys. Rev. B **23**, 5048 (1981); A. Swane and O. Gunnarson, Phys. Rev. Lett. **65**, 1148 (1990).

[40] A.B. Shick, A.I. Liechtenstein, and W.E. Pickett, Phys. Rev. B **60**, 10 763 (1999).

[41] A. Georges, G. Kotliar, W. Krauth, and M.J. Rozenberg, Rev. Mod. Phys. **68**, 13 (1996).